J. Fluid Mech. (2009), *vol.* 628, *pp.* 339–356. © 2009 Cambridge University Press
doi:10.1017/S0022112009006247 Printed in the United Kingdom

Effects of axisymmetric strain on a passive scalar field: modelling and experiment

A. GYLFASON[1]† AND Z. WARHAFT[2]

[1]School of Science and Engineering, Reykjavik University, IS-103, Reykjavik, Iceland
[2]Sibley School of Mechanical and Aerospace Engineering, Cornell University, Ithaca, NY 14853, USA

(Received 31 March 2008 and in revised form 21 January 2009)

Homogeneous, approximately isotropic turbulence at two Taylor-scale Reynolds numbers, $R_\lambda = 50,\ 190$, with a mean transverse temperature gradient is passed through an axisymmetric contraction. The effects of the straining on the velocity field, and on the passive scalar field, are investigated within the contraction as are the effects of releasing the strain in the post-contraction region. Components of the fluctuating velocity and scalar gradient covariance are measured in order to understand their relation to the large-scale anisotropy of the flow. The scale-dependent spectral evolution of the scalar is also determined. A tensor model is constructed to predict the evolution of the fluctuating scalar gradient covariance. The model constants are determined in the post-contraction relaxation region, where the flow geometry does not vary. The model is shown to perform well throughout the flow, even in the contraction in which the geometry varies. Rapid distortion theory is applied to the scalar field in the contraction, and its solutions are compared to the experimental results.

1. Introduction

Understanding the dynamics of the small-scale turbulent velocity structure is central to proper turbulence modelling, such as large-eddy simulation (LES; Meneveau & Katz 2000) and Reynolds-averaged Navier–Stokes (RANS; Hanjalic 1994). Further, the small-scale structure of a scalar is central to many engineering applications, such as mixing (e.g. Warhaft 2000; Dimotakis 2005), reactions and combustion (e.g. Peters 1983; Pope 1990; O'Young & Bilger 1997; Bilger 2004).

The objective of this work is to investigate the effects of straining on a passive scalar field. To address this we pass approximately isotropic wind-tunnel turbulence, with an imposed transverse passive temperature gradient to provide the scalar fluctuations, through an axisymmetric contraction. After the straining the turbulence is allowed to relax towards its preferred state. In both the straining and the relaxation regions the small-scale statistics are measured and compared with analytical results. We consider the components of the scalar dissipation and their relation to the large-scale structure of the flow field. The measurements show that the components of the fluctuating scalar gradient covariance tensor are highly dependent on the velocity structure, indicating that the assumption of approximate isotropy at small scales in the scalar field only applies to special cases. Our study stems from the earlier work of Ayyalasomayajula & Warhaft (2006) which focused purely on the velocity field.

---

† Email address for correspondence: armann@ru.is

Mean straining occurs in any turbulent boundary layer and in many internal flows, such as nozzles and diffusers. In the earliest investigations, researchers (Prandtl 1933; Taylor 1933; Batchelor 1953) realized that when the straining motion is sufficiently rapid, the nonlinear and viscous forces in the Navier–Stokes equations become negligible, and the flow equations become linear. This led to the introduction of rapid distortion theory (RDT), which has been applied to a variety of flow geometries (e.g. see Savill 1987; Hunt & Carruthers 1990). Primarily due to its simplicity compared to solving the full Navier–Stokes equations, RDT is widely used in engineering applications in which turbulent flows undergo straining motion. The basic assumption of RDT is that in the rapid distortion limit, each Fourier mode describing the flow field evolves independently.

In the rapid distortion limit the scalar equation becomes particularly simple (see § 2.2). RDT predictions for the scalar field have been studied extensively (e.g. see Townsend 1976), for both fixed strain rate and variable straining, and analytical expressions for the scalar spectrum and velocity–scalar co-spectrum have been derived for some geometries (Wyngaard 1988; Rogers 1991; Rahai & LaRue 1995). In this study we rederive the evolution of the scalar spectrum according to RDT in the simple case of the axisymmetric contraction and compare it with experiments.

The relaxation of highly anisotropic turbulence also has been investigated extensively (Rotta 1951; Launder, Reece & Rodi 1975; Lumley & Newman 1977; Newman, Launder & Lumley 1981; Chung & Kim 1995; Reynolds & Kassinos 1995; Ayyalasomayajula & Warhaft 2006). However, there appears to be very little work on passive scalars and their derivative moments for the simple, but important, flow geometry studied here. Previous experiments have focused on practical applications in more complex flows (Rogers 1991; Rahai & LaRue 1995). Here a tensor model is introduced to describe the evolution of the components of the scalar dissipation. The model constants are determined in the post-straining region, where the geometry of the flow is fixed, while the flow evolves from anisotropic initial state towards a more isotropic state. The model is then shown to perform well in the straining region. The model constants give important insight into the relation between the structure of the passive scalar field and the velocity field. The authors believe that the model could be useful in refining models of scalar dissipation as well as aiding with design of geometry in which reactive flows occur.

2. Governing equations

The main objective of this work is to study the passive scalar field. The background velocity field is documented, for completeness. For the details of the governing equations for the straining as well as their modification for RDT and the post-straining relaxation we refer to Ayyalasomayajula & Warhaft (2006).

2.1. *Equations for the passive scalar*

A conserved passive scalar θ is a non-reactive diffusive contaminant that is present in such low concentration that it has no dynamical effect on the fluid motion itself. The equation describing the scalar transport is given by

$$\frac{\mathrm{D}\theta}{\mathrm{D}t} = \Gamma \nabla^2 \theta, \tag{2.1}$$

where $\mathrm{D}/\mathrm{D}t \equiv \partial/\partial t + U_i \partial/\partial x_i$ is the material derivative following a fluid particle; U_i is the instantaneous velocity; θ is the scalar concentration from here on taken to be temperature, which is assumed to have small enough variations so that the material properties of the fluid are constant; and Γ is the thermal diffusivity.

The equation for the scalar fluctuations, $\theta' = \theta - \langle\theta\rangle$, can be shown to be (Tennekes & Lumley 1972)

$$\frac{\mathrm{D}\theta'}{\mathrm{D}t} = -u_k \frac{\partial\langle\theta\rangle}{\partial x_k} + \frac{\partial}{\partial x_k}\langle u_k\theta'\rangle + \Gamma\frac{\partial^2\theta'}{\partial x_k \partial x_k}. \tag{2.2}$$

Here, $u_i = U_i - \langle U_i\rangle$ is the fluctuating velocity component, and the angle brackets represent a local ensemble or time average. From (2.2) it can be shown that the equation for the evolution of the scalar variance $\langle\theta'^2\rangle$ is

$$\frac{\bar{\mathrm{D}}\langle\theta'^2\rangle}{\bar{\mathrm{D}}t} + \frac{\partial}{\partial x_k}\left(\langle u_k\theta'^2\rangle - \Gamma\frac{\partial\langle\theta'^2\rangle}{\partial x_k}\right) = -2\langle u_k\theta'\rangle\frac{\partial\langle\theta\rangle}{\partial x_k} - 2\Gamma\left\langle\frac{\partial\theta'}{\partial x_k}\frac{\partial\theta'}{\partial x_k}\right\rangle, \tag{2.3}$$

where $\bar{\mathrm{D}}/\bar{\mathrm{D}}t = \partial/\partial t + \langle U_i\rangle\partial/\partial x_i$ is the mean substantial derivative. The last term on the right-hand side of (2.3) is the scalar dissipation rate, which from here on will be denoted as ε_θ.

Taking the gradient of (2.2) we obtain the following relation for the fluctuating scalar gradients $\zeta_j \equiv \partial\theta'/\partial x_j$:

$$\frac{\mathrm{D}\zeta_j}{\mathrm{D}t} + \zeta_k\frac{\partial U_k}{\partial x_j} = -\frac{\partial u_k}{\partial x_j}\frac{\partial\langle\theta\rangle}{\partial x_k} - u_k\frac{\partial^2\langle\theta\rangle}{\partial x_k\partial x_j} + \frac{\partial}{\partial x_j}\langle u_k\zeta_k\rangle + \Gamma\frac{\partial^2\zeta}{\partial x_k\partial x_k}. \tag{2.4}$$

Multiplying (2.4) by ζ_i, adding the resulting equation to itself, interchanging the subscripts i and j and taking an ensemble average, we obtain the following equation for the fluctuating scalar covariance tensor:

$$\begin{aligned}\frac{\bar{\mathrm{D}}\langle\zeta_i\zeta_j\rangle}{\bar{\mathrm{D}}t} + \frac{\partial}{\partial x_k}\langle u_k\zeta_i\zeta_j\rangle &= -\frac{\partial\langle\theta\rangle}{\partial x_k}\left\langle\frac{\partial u_k}{\partial x_j}\zeta_i + \frac{\partial u_k}{\partial x_i}\zeta_j\right\rangle \\ &- \left\langle\zeta_i\zeta_k\frac{\partial u_k}{\partial x_j} + \zeta_j\zeta_k\frac{\partial u_k}{\partial x_i}\right\rangle - \left(\langle\zeta_i\zeta_k\rangle\frac{\partial\langle U_k\rangle}{\partial x_j} + \langle\zeta_j\zeta_k\rangle\frac{\partial\langle U_k\rangle}{\partial x_i}\right) + \Gamma\frac{\partial^2}{\partial x_k\partial x_k}\langle\zeta_i\zeta_j\rangle \\ &- \left(\langle\zeta_i u_k\rangle\frac{\partial^2\langle\theta\rangle}{\partial x_k\partial x_j} + \langle\zeta_j u_k\rangle\frac{\partial^2\langle\theta\rangle}{\partial x_k\partial x_i}\right) - 2\Gamma\left\langle\frac{\partial\zeta_i}{\partial x_k}\frac{\partial\zeta_j}{\partial x_k}\right\rangle.\end{aligned} \tag{2.5}$$

This equation can be simplified considerably by considering relative magnitudes of the different terms (see below).

2.2. *The effects of the distortion on the scalar spectrum*

Equation (2.1) is considerably simplified for a homogeneous passive scalar field evolving according to the RDT framework (e.g. see Pope 2000):

$$\frac{\bar{\mathrm{D}}\theta}{\bar{\mathrm{D}}t} = 0. \tag{2.6}$$

The flow presented in this study is approximately homogeneous, particularly over small increments. Thus it is useful to compare the experimental results to the idealized case of homogeneous axisymmetrically strained turbulence. For such flow, we can artificially impose periodicity, which allows us to investigate the spectral evolution of the scalar field. The evolution equation of the discrete Fourier coefficient follows directly from equation (2.6):

$$\frac{\mathrm{d}\hat{\theta}_{\hat{\kappa}}}{\mathrm{d}t} + \langle U_j\rangle \mathrm{i}\hat{\kappa}_j\hat{\theta}_{\hat{\kappa}} = 0 \tag{2.7}$$

Here, $\hat{\theta}_{\hat{\kappa}}$ is the time-dependent Fourier coefficient at wavenumber $\hat{\boldsymbol{\kappa}}$. Further manipulation yields

$$\frac{\mathrm{d}}{\mathrm{d}t}(\hat{\theta}_{\hat{\kappa}}\hat{\theta}^*_{\hat{\kappa}})=0, \tag{2.8}$$

where $\hat{\theta}^*_{\hat{\kappa}}$ is the complex conjugate of $\hat{\theta}_{\hat{\kappa}}$; i.e. the product $(\hat{\theta}_{\hat{\kappa}}\hat{\theta}^*_{\hat{\kappa}})$ is independent of time in the rapid distortion limit.

The scalar field, written in terms of its Fourier components, is

$$\theta(\boldsymbol{x},t)=\sum_{\hat{\kappa}}\hat{\theta}_{\hat{\kappa}}\mathrm{e}^{\mathrm{i}\hat{\boldsymbol{\kappa}}\cdot\boldsymbol{x}}+\boldsymbol{g}\cdot\boldsymbol{x}, \tag{2.9}$$

where $\boldsymbol{g}(t)$ is the mean thermal gradient of the flow.

Applying (2.6) to the thermal field in (2.9) we obtain the following relations for the time evolution of the wavenumber and the mean thermal gradient:

$$\frac{\mathrm{d}\hat{\kappa}_i}{\mathrm{d}t}+\hat{\kappa}_k\frac{\partial\langle U_k\rangle}{\partial x_i}=0, \tag{2.10}$$

$$\frac{\mathrm{d}g_i}{\mathrm{d}t}+g_k\frac{\partial\langle U_k\rangle}{\partial x_i}=0. \tag{2.11}$$

To proceed we investigate the geometry of the mean flow. For an axisymmetric contraction the mean velocity gradient tensor is given by

$$\frac{\partial\langle U_i\rangle}{\partial x_j}=\begin{bmatrix} S_\lambda & 0 & 0 \\ 0 & -\frac{1}{2}S_\lambda & 0 \\ 0 & 0 & -\frac{1}{2}S_\lambda \end{bmatrix}, \tag{2.12}$$

where $S_\lambda=S_\lambda(t)$ is the principal mean strain, the largest eigenvalue of the mean rate of strain tensor, defined by $\bar{S}_{ij}\equiv(\partial\langle U_i\rangle/\partial x_j+\partial\langle U_j\rangle/\partial x_i)/2$. The characteristic mean strain, used to parameterize the strain rate, is defined as $S=(2\bar{S}_{ij}\bar{S}_{ij})^{1/2}$. For the axisymmetric contraction it follows that $S=\sqrt{3}S_\lambda$.

Due to the simple form of $\partial\langle U_i\rangle/\partial x_j$, each component of the wavenumber evolves independently according to (2.10):

$$\hat{\kappa}_{(i)}(t)=\hat{\kappa}^\circ_{(i)}\mathrm{e}^{-A_{(i)}\int_0^t S_\lambda(t)\mathrm{d}t}=\hat{\kappa}^\circ_{(i)}\mathrm{e}^{-A_{(i)}c}. \tag{2.13}$$

Here, $\hat{\boldsymbol{\kappa}}^\circ$ is the initial wavenumber that describes the thermal field at time $t=0$; $\boldsymbol{A}=[1,-1/2,-1/2]^T$; and c is a dimensionless time defined as $\mathrm{d}c=S_\lambda\mathrm{d}t$. (Note that summation over indices does not apply when they appear inside parentheses.)

We now focus our attention to the spectral evolution of the scalar field. The scalar spectrum (scalar function of the three-dimensional wavenumber) is given by

$$\Phi(\boldsymbol{\kappa},t)=\sum_{\hat{\kappa}}\delta(\boldsymbol{\kappa}-\hat{\boldsymbol{\kappa}})\langle\hat{\theta}^*_{\hat{\kappa}}\hat{\theta}_{\hat{\kappa}}\rangle \tag{2.14}$$

Equation (2.8) implies that the scalar spectrum maintains it form during the straining but is shifted in wavenumber:

$$\Phi(\boldsymbol{\kappa},c)=\Phi(\boldsymbol{\kappa}^\circ,0). \tag{2.15}$$

Our experimental methods are limited to resolving the spectrum function of the longitudinal wavenumber $E^\theta(\kappa_1,t)$ defined by

$$E^\theta(\kappa_1,t)=\iint_{-\infty}^{\infty}\Phi(\boldsymbol{\kappa},t)\,\mathrm{d}\kappa_2\,\mathrm{d}\kappa_3. \tag{2.16}$$

In light of (2.15) the one-dimensional spectra before and after the contraction are

$$E^{\theta}(\kappa_1, c) = \mathrm{e}^{c} E^{\theta}(\kappa_1^{\circ}, 0). \tag{2.17}$$

Equation (2.15) allows us to evaluate the evolution of the scalar variance as well as the scalar covariance variance tensor as the flow passes through the contraction. The scalar variance evolves according to

$$\langle \theta'^2 \rangle_t = \langle \theta'^2 \rangle_{t=0}, \tag{2.18}$$

and the fluctuating scalar covariance is given by

$$\left\langle \frac{\partial \theta'}{\partial x_{(i)}} \frac{\partial \theta'}{\partial x_{(j)}} \right\rangle_t = \mathrm{e}^{-(A_{(i)}+A_{(j)})c} \left\langle \frac{\partial \theta'}{\partial x_{(i)}} \frac{\partial \theta'}{\partial x_{(j)}} \right\rangle_{t=0}. \tag{2.19}$$

It is demonstrated below that in our experiments the scalar spectra deviate from RDT predictions at the highest wavenumbers. This is a direct consequence of the non-rapid effects at the higher wavenumbers.

2.3. *Model for the evolution of the scalar covariance tensor*

For the present flow, after the strain has been released, (2.5) reduces to

$$\frac{\mathrm{d}\langle \zeta_i \zeta_j \rangle}{\mathrm{d}t} = -\left\langle \zeta_i \zeta_k \frac{\partial u_k}{\partial x_j} + \zeta_j \zeta_k \frac{\partial u_k}{\partial x_i} \right\rangle - 2\Gamma \left\langle \frac{\partial \zeta_i}{\partial x_k} \frac{\partial \zeta_j}{\partial x_k} \right\rangle. \tag{2.20}$$

Here, we have assumed homogeneity to drop the second term on the left-hand side of (2.5), as well as the third through fifth terms on the right-hand side. Scaling indicates that the second term on the right-hand side of (2.5), involving fluctuating gradients only, should be at least ℓ/λ greater than the first term, involving the mean temperature gradient. Here, ℓ is the integral scale and λ is the Taylor microscale of the flow. Thus although the mean temperature gradient is responsible for the fluctuating scalar covariance, it does not appear explicitly in (2.20). This is similar to the situation for the mean square vorticity budget. Here the mean square vorticity fluctuations are approximately independent of the mean flow (Tennekes & Lumley 1972, p. 86). We note that scaling strictly applies only for high Reynolds numbers. However, re-analysis of our previous data (Gylfason & Warhaft 2004) with a comparable mean temperature gradient indicate that even at $R_\lambda = 50$ the first term on the right-hand side of (2.5) is an order of magnitude smaller than the second term.

Defining the quantities R_{ij} and ε_{ij}^{ζ} to be the first and the second term on the right-hand side of (2.20) and the quantity $C_{ij} = \langle \zeta_i \zeta_j \rangle$, (2.20) becomes

$$\frac{\mathrm{d}C_{ij}}{\mathrm{d}t} = -R_{ij} - \varepsilon_{ij}^{\zeta}. \tag{2.21}$$

We now seek to produce a non-dimensional relationship for the fluctuating scalar covariance tensor. Dividing (2.21) by C_{kk} yields the following:

$$\frac{\mathrm{d}}{\mathrm{d}t}\left(\frac{C_{ij}}{C_{kk}}\right) = -\frac{\varepsilon_{kk}^{\zeta}}{C_{kk}} \left\{ \frac{R_{ij}}{\varepsilon_{kk}^{\zeta}} + \frac{\varepsilon_{ij}^{\zeta}}{\varepsilon_{kk}^{\zeta}} - \frac{C_{ij}}{C_{kk}} \left(\frac{R_{kk}}{\varepsilon_{kk}^{\zeta}} + 1 \right) \right\}. \tag{2.22}$$

The prefactor $\varepsilon_{kk}^{\zeta}/C_{kk}$ is used in order to define the dimensionless time $\mathrm{d}s = (\varepsilon_{kk}^{\zeta}/C_{kk})\,\mathrm{d}t$. (The relationship between s and $t\varepsilon/k$, where k is the turbulent kinetic energy, is discussed below.)

Equation (2.22) allows us to construct a simple tensor model, which aims to capture the important aspects of our experimental findings on the evolution of the scalar covariance. To achieve this, the tensors R_{ij} and ε^{ζ}_{ij}, are modelled as functions of the measurable flow parameters.

The source term and the gradient dissipation term may be written as a second-order tensor function of the flow parameters:

$$R_{ij} + \varepsilon^{\zeta}_{ij} = F_{ij}\big(C_{kl}, \langle u_k u_l \rangle, \varepsilon, \nu, \varepsilon^{\zeta}_{kk}, Pr\big). \tag{2.23}$$

In this representation it has been assumed that R_{ij} and ε^{ζ}_{ij} depend primarily on the C_{ij} and $\langle u_i u_j \rangle$, whereas the dependence on the mean scalar gradient $\partial \langle \theta \rangle / \partial x_i$ has been omitted.

The invariance principle allows us to write

$$R_{ij} + \varepsilon^{\zeta}_{ij} = C_{kl} H_{ijkl}\big(\langle u_m u_n \rangle, \varepsilon, \nu, Pr, \varepsilon^{\zeta}_{kk}\big), \tag{2.24}$$

where H_{ijkl} is a fourth-order tensor constructed from $\langle u_i u_j \rangle$ and δ_{ij}. We propose the following model for the terms on the right-hand side of (2.22):

$$\frac{R_{ij}}{\varepsilon^{\zeta}_{kk}} + \frac{\varepsilon^{\zeta}_{ij}}{\varepsilon^{\zeta}_{kk}} = \frac{1}{3} f^{(1)} \delta_{ij} + f^{(2)} \frac{C_{ij}}{C_{kk}} + f^{(3)} \frac{S_{ij}}{S_{kk}}. \tag{2.25}$$

Here $S_{ij} = \langle u_i u_j \rangle$; $f^{(1)}, f^{(2)}, f^{(3)}$ are scalar functions of the Reynolds number and Prandtl number. We are unable to estimate the importance of the higher-order terms $S_{il} C_{jl} + S_{jl} C_{il}$, S^2_{ij}, $S^2_{il} C_{jl} + S^2_{jl} C_{il}$. Further refinement of the model would allow for dependence of these higher-order terms.

Rewriting (2.22) in terms of departure from isotropy yields

$$\frac{\mathrm{d}}{\mathrm{d}s} C'_{ij} = -\left\{ R'_{ij} + \varepsilon^{\zeta\prime}_{ij} - C'_{ij} \left(\frac{R_{kk}}{\varepsilon^{\zeta}_{kk}} + 1 \right) \right\}, \tag{2.26}$$

where $C'_{ij} = C_{ij}/C_{kk} - \delta_{ij}/3$, $R'_{ij} = R_{ij}/\varepsilon^{\zeta}_{kk} - R_{kk}/\varepsilon^{\zeta}_{kk}\delta_{ij}/3$ and $\varepsilon^{\zeta\prime}_{ij} = \varepsilon^{\zeta}_{ij}/\varepsilon^{\zeta}_{kk} - \delta_{ij}/3$. Applying the model in (2.25) to (2.26) we obtain

$$\frac{\mathrm{d}}{\mathrm{d}s} C'_{ij} + f^{(4)} C'_{ij} = -f^{(3)} b_{ij}, \tag{2.27}$$

where $b_{ij} = S_{ij}/S_{kk} - \delta_{ij}/3$ is the fluctuating velocity anisotropy tensor and $f^{(4)} = -(f^{(1)} + f^{(3)})$. Note that in the current experiments we only resolve the ε^{ζ}_{11} component of the tensor ε^{ζ}_{ij}. As a result, when determining the time s we assume that $\varepsilon^{\zeta}_{kk} = 3\varepsilon^{\zeta}_{11}$.

The model in (2.25) can be used for varying flow geometry by including the third term on the right-hand side of (2.5), which quickly becomes important when mean straining is present. This approach is useful when the straining is not sufficiently rapid to apply the results of § 2.2. The equation becomes

$$\frac{\mathrm{d}}{\mathrm{d}s} C'_{ij} = -f^{(4)} C'_{ij} - f^{(3)} b_{ij} + M_{ij}, \tag{2.28}$$

where the tensor M_{ij} is defined by the following:

$$M_{ij} = \frac{C_{kk}}{\varepsilon^{\zeta}_{kk}} \left\{ \left(C'_{ij} + \frac{1}{3}\delta_{ij} \right) 2C'_{lm} \frac{\partial \langle U_m \rangle}{\partial x_l} - C'_{il} \frac{\partial \langle U_l \rangle}{\partial x_j} - C'_{jl} \frac{\partial \langle U_l \rangle}{\partial x_i} - \frac{2}{3} \bar{S}_{ij} \right\}. \tag{2.29}$$

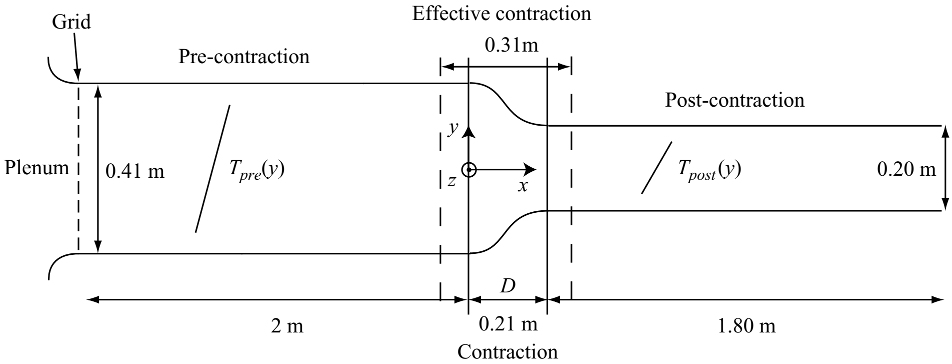

FIGURE 1. A sketch of the wind-tunnel facility. See §4.1 for the definition of effective contraction.

3. Apparatus

Turbulence is generated in our vertical wind-tunnel facility (Sirivat & Warhaft 1983), by means of active (Makita 1991; Mydlarski & Warhaft 1996) and passive grids, both with mesh sizes of $M = 5.08$ cm. For the passive grid, the Reynolds number is $R_\lambda \approx 50$ in the pre-contraction stream, whereas for the active grid it is $R_\lambda \approx 190$. The turbulent flow is allowed to decay for 40 mesh lengths before passing through a 4:1 axisymmetric contraction which is identical to that described in Warhaft (1980) and Ayyalasomayajula & Warhaft (2006).

A linear temperature profile is generated in the tunnel plenum using differentially heated ribbons (a ‘toaster), before passing through a series of honeycomb, screens and finally a flow-conditioning contraction, which produces nearly laminar flow. The turbulence is generated by the active or passive grid at the entrance to the test section, and the temperature fluctuations are generated by the action of the turbulent eddies on the mean temperature gradient, as in Sirivat & Warhaft (1983). The temperature gradient was measured at several locations (see below), before and after the contraction region with a thermocouple rake, consisting of 6–11 thermocouples. A sketch of the facility is shown in figure 1.

The temperature fluctuations were measured with derivative probes, two parallel wires, connected to DC temperature bridges. Platinum wires, diameter $D = 0.63$ μm with an etched length of 0.32 mm were used. The distance between the two wires was $\Delta = 1$ mm and $\Delta = 0.6$ mm. The smaller separation was used in the higher-Reynolds-number active grid flow, for which the Kolmogorov microscale was $\eta = 0.28$ mm, while the larger separation was used for the passive grid flow, where $\eta = 0.41$ mm (see table 1). The transverse derivative (y) was obtained by subtracting the signals from the two wires, while the longitudinal derivatives (x) as well as other longitudinal statistics were obtained using Taylor’s frozen flow hypothesis for each of the wires independently. Data of figure 2 of Gylfason, Ayyalasomayajula & Warhaft (2004) suggest Taylor’s hypothesis holds well for the turbulence intensities observed in the present work.

Velocity fluctuations were measured with TSI 1241 X-array probes connected to Dantec 55M01 constant temperature anemometers. Tungsten wires of 3.05 μm diameter were used, with an etched length of 0.6 mm. For further information on our temperature and velocity anemometry we refer the reader to Mydlarski & Warhaft (1998).

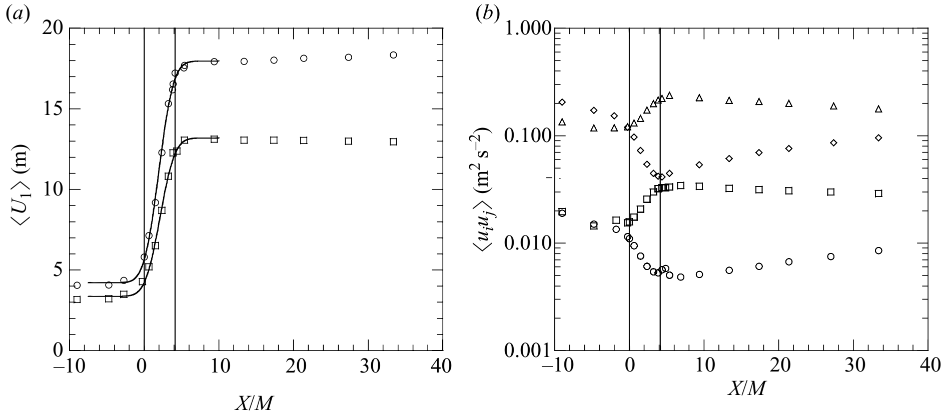

FIGURE 2. (*a*) The mean velocity $\langle U_1 \rangle$ versus X/M. Circles: passive grid; squares: active grid. The solid lines show an error function curve fit to the data. (*b*) Components of the Reynolds stresses $\langle u_i u_j \rangle$ versus X/M. Passive grid: circles, $\langle u_1 u_1 \rangle$; squares, $\langle u_2 u_2 \rangle$. Active grid: diamonds, $\langle u_1 u_1 \rangle$; triangles, $\langle u_2 u_2 \rangle$. The vertical lines indicate the location of the contraction in both figures.

Temperature and velocity signals were band-pass filtered and digitized with a 12 bit A/D converter. The high-pass filter was set at $f_h = 0.01$ Hz, while the low-pass filter frequency was varied $f_l = 2500$–$12\,000$ Hz, depending on flow parameters. The sampling frequency was set at $f_s = 2 f_l$. Both temperature and velocity statistics were calculated from data series containing 8×10^6 points.

4. Results

Table 1 shows the flow parameters for the two conditions studied. Notice that the velocity field has undergone slight straining before entering the contraction, with the result that the fluctuating velocity component in the longitudinal direction (u) is smaller than the transverse component (v) for the passive grid. This is discussed below. Further upstream from the contraction the velocity field is close to isotropic, consistent with the observation of Comte-Bellot & Corrsin (1966). For the active grid, which departs more markedly from isotropy (Mydlarski & Warhaft 1996), the pre-contraction straining reduces the anisotropy of the flow field but does not produce isotropy.

Figure 2(*a*,*b*) show the evolution of the mean velocity and the Reynolds stresses along the test section of the wind-tunnel. The effects of the contraction are felt both before the flow enters the contraction and after it exits. The velocity profile is smooth and is found to be well approximated by an error function.

Figure 3(*a*) shows the mean temperature gradients for the active and passive grids. For the higher-Reynolds-number flow (active grid) the gradient decays noticeably due to the intense turbulent mixing (Mydlarski & Warhaft 1998, p. 142). However the ratio $(\partial T/\partial x)/(\partial T/\partial y) \sim 0.05$; thus production effects in the x direction are small compared with those in the transverse, y, direction, and we will show that the active grid results are qualitatively similar to the passive grid, for which $(\partial T/\partial x)/(\partial T/\partial y) \approx 0$.

Figure 3(*b*) shows the evolution of the ratio of the scalar variance and the mean thermal gradient as a function of normalized distance, measured from the beginning of the test section. The normalized scalar variance decreases in the contraction by

	Active grid		Passive grid	
	Before	After	Before	After
M (cm)	5.08		5.08	
U ($\mathrm{m\,s^{-1}}$)	3.7	13.0	4.7	17.7
$\mathrm{d}T/\mathrm{d}y$ ($\mathrm{K\,m^{-1}}$)	3.61	6.85	5.5	11.0
$\langle u^2\rangle$ ($\mathrm{m^2\,s^{-2}}$)	0.153	0.045	0.013	0.005
$\langle v^2\rangle$ ($\mathrm{m^2\ s^{-2}}$)	0.119	0.238	0.016	0.033
$k=\frac{1}{2}(\langle u^2\rangle+2\langle v^2\rangle)$ ($\mathrm{m^2\ s^{-2}}$)	0.195	0.260	0.023	0.036
$\langle\theta'^2\rangle$ (K^2)	0.072	0.075	0.009	0.011
$\ell=\left(\frac{2}{3}k\right)^{3/2}/\varepsilon$ (m)	0.091	0.273	0.020	0.266
$\lambda=\left(\frac{2}{3}k/(\varepsilon/15\nu)\right)^{1/2}$ (mm)	7.77	12.1	5.99	19.5
$\eta=(\nu^3/\varepsilon)^{1/4}$ (mm)	0.289	0.336	0.435	0.702
$\tau_\eta=(\nu/\varepsilon)^{1/2}$ (ms)	5.57	7.52	12.7	33.0
$\varepsilon=\nu\left(5\langle(\frac{\partial u}{\partial x})^2\rangle+5\langle(\frac{\partial v}{\partial x})^2\rangle\right)$ ($\mathrm{m^2\,s^{-3}}$)	0.484	0.265	0.094	0.014
$\varepsilon_\theta=2\Gamma\left(\left\langle(\frac{\partial\theta}{\partial x})^2\right\rangle+2\langle(\frac{\partial\theta}{\partial y})^2\rangle\right)$ ($\mathrm{K^2\,s^{-1}}$)	0.189	0.262	0.037	0.067
$Re_\ell=\left(\frac{2}{3}k\right)^{1/2}\ell/\nu$	2190	7585	163	2667
$R_\lambda=\left(\frac{2}{3}k\right)^{1/2}\lambda/\nu$	187	336	49	200

TABLE 1. Flow parameters for the two conditions studied. Flow parameters for the two grids are listed both before (at $X/M=-2$) and after the contraction (at $X/M=5.5$), where M is the mesh length (see figure 1). The physical contraction is located 40 mesh lengths from the turbulence generating grid, between $0\leqslant X/M\leqslant 4.13$, while the effective contraction (see figure 4) is between $-1\leqslant X/M\leqslant 5$.

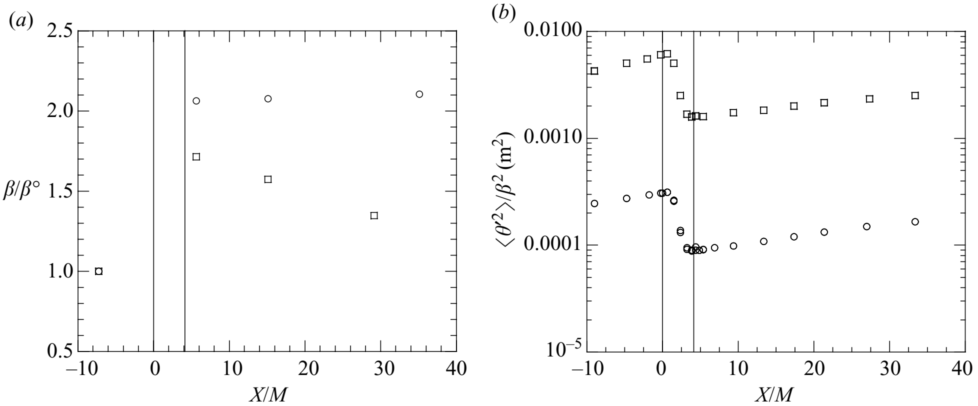

FIGURE 3. (a) The mean temperature gradient β normalized by the mean temperature gradient in the pre-contraction region at $X/M=-7.25$, β° versus X/M. (b) The scalar variance divided by the local mean scalar gradient $\langle\theta'^2\rangle/\beta^2$ versus X/M. For both figures, circles: passive grid; squares: active grid; the solid vertical lines show the location of the contraction.

four, due to the doubling of the mean gradient. We will show below (figure 6) that the variance itself remains constant.

4.1. *Straining region*

We now focus our attention on the straining region in the flow. Both velocity and scalar measurements were conducted inside the contraction.

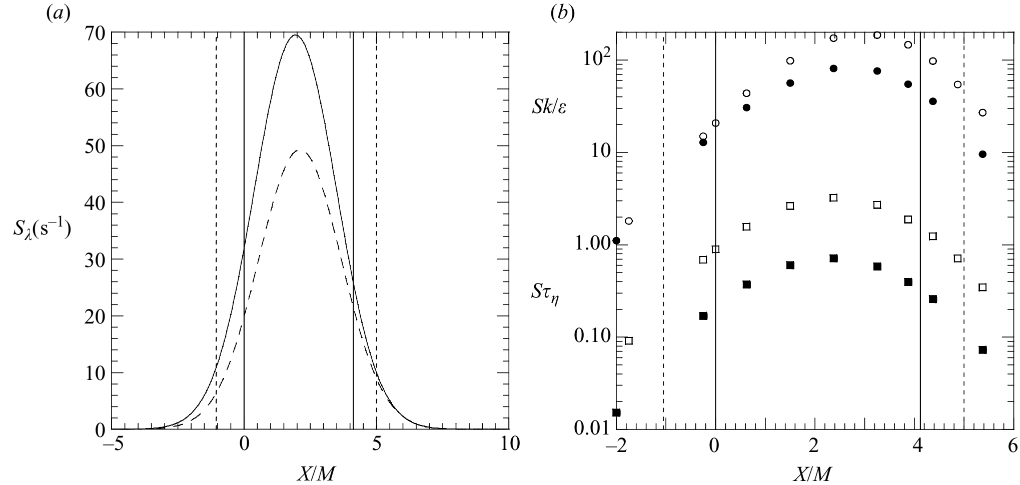

FIGURE 4. (*a*) The principal mean strain rate parameter S_λ versus X/M. Solid line: passive grid; dashed line: active grid. (*b*) The strain parameters Sk/ε (circles) and $S\tau_\eta$ (squares) versus X/M. Open symbols: passive grid; filled symbols: active grid. The solid vertical lines indicate the contraction region, while the dashed vertical lines show the effective straining region.

4.1.1. *Velocity field*

The principal mean strain rate S_λ characterizes the mean flow through the straining region. For an axisymmetric contraction it is given by $S_\lambda = \partial\langle U_1\rangle/\partial x$. As shown above the mean velocity profile through the contraction is well approximated by the error function, from which S_λ is determined. Note that the strain is non-uniform; hence statistics are represented as functions of c defined by $\mathrm{d}c = S_\lambda \mathrm{d}t$, and $c = 0$ occurs at the beginning of the effective straining region (see below). Inhomogeneity due to the variable strain is not believed to have significant effect on the small-scale statistics studied in this paper (see also Ayyalasomayajula & Warhaft 2006).

Figure 2(*a,b*) showed that some straining also occurs outside the contraction region, due to viscous and boundary-layer effects. As a result we base our analysis on the effective straining region taken to be between the locations x_1, x_2 in which $(\langle U_1\rangle_{x_1,x_2} - \langle U_1\rangle_i)/(\langle U_1\rangle_f - \langle U_1\rangle_i) = 0.025, 0.975$, where $\langle U_1\rangle_i$ is the pre-contraction velocity and $\langle U_1\rangle_f$ is the post-contraction velocity. Figure 4(*a,b*) indicate the extent of this region. The effective straining region is therefore between $X/M = -1.0$ and $X/M = 5.0$.

Figure 4(*b*) shows the shear parameters as functions of distance in the contracting stream. The value of the strain parameters Sk/ε and $S\tau$ are essential in determining the importance of various terms in the evolution equations for the scalar field as well as the velocity field. In order for RDT to apply the parameters must satisfy $Sk/\varepsilon \gg 1$ and $S\tau \gg 1$. In our measurements the first constraint is weakly satisfied ($Sk/\varepsilon > 10$). Here, RDT predicts the behaviour of the large-scale statistics reasonably well. The second constraint is not satisfied, and the effect of the strain on the small scales is not rapid (Ayyalasomayajula & Warhaft 2006).

The evolution of the velocity anisotropy tensor, b_{ij}, in the straining region is shown in figure 5. Both the active and the passive grids display very similar responses to the straining. The production for the longitudinal component is negative, $P_{11} = -\langle u_1^2\rangle S_\lambda$, while it is positive for the transverse components, e.g. $P_{(ii)} = \langle u_{(i)}^2\rangle S_\lambda/2$ ($i = 2, 3$). In the early stages the production of the transverse components is expected to be less than exponential due to the redistribution term in the RDT equations (Pope 2000); however at long times the effects of the redistribution are diminished. The long-time

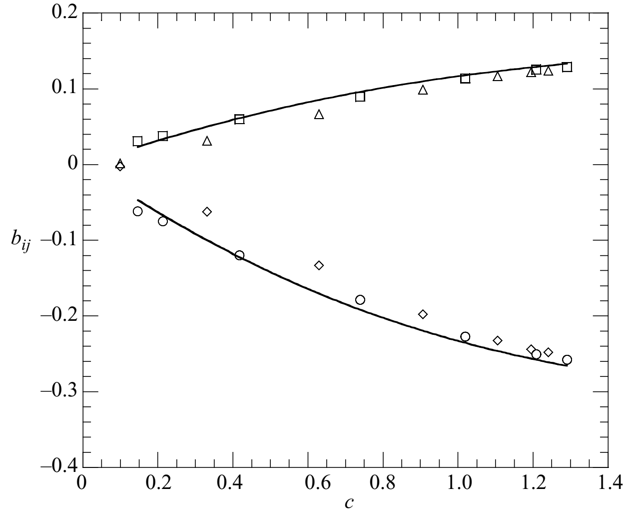

FIGURE 5. The evolution of the anisotropy tensor b_{ij} in the straining region as a function of c. (Note that $c = 0$ at the beginning of the effective straining region, $X/M = -1.0$.) Passive grid: circles, b_{11}; squares, b_{22}. Active grid: diamonds, b_{11}; triangles, b_{22}. The lines are the long-time predictions of RDT (see the text).

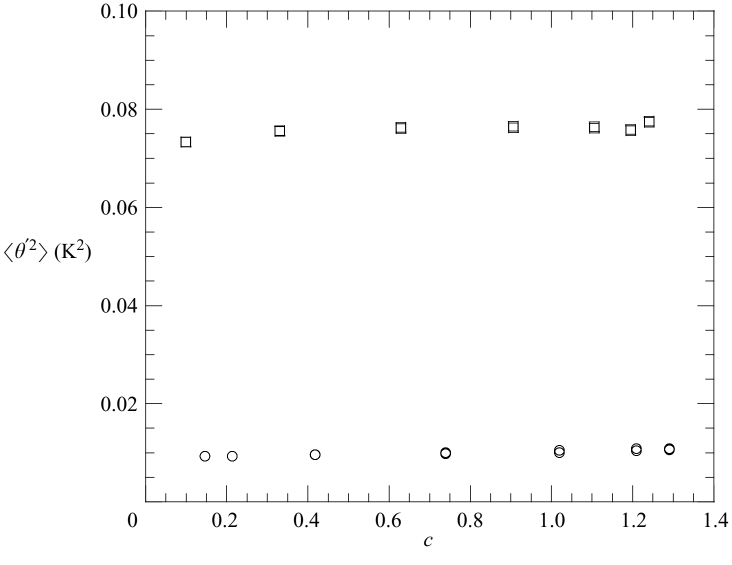

FIGURE 6. The temperature fluctuation variance $\langle \theta'^2 \rangle$ versus c in the contraction. Circles: passive grid; squares: active grid.

prediction is shown in figure 5, assuming isotropic velocity field at time $c = 0$, and the agreement with the experimental data is found to be very good. Note the difference in initial conditions of the flow isotropy at the beginning of the effective contraction for the passive grid and active grid flow (see figure 2(*b*) and table 1).

4.1.2. *Scalar field*

The evolution of the temperature variance divided by the local temperature gradient was shown in figure 3. Figure 6 shows that the non-normalized temperature variance

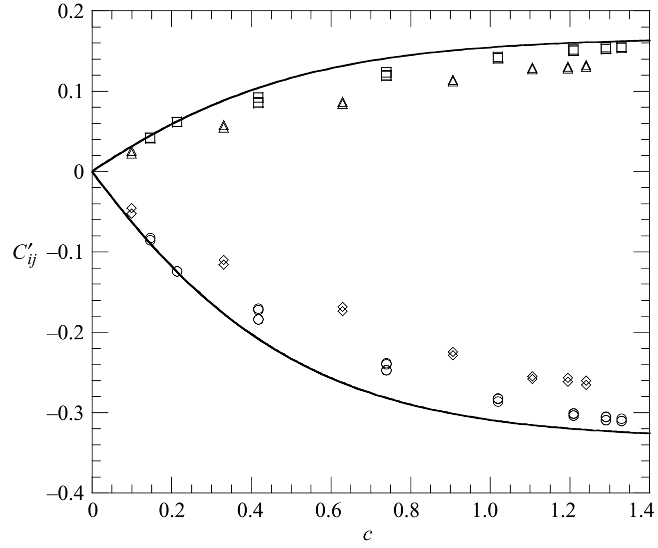

FIGURE 7. The fluctuating temperature gradient anisotropy tensor C'_{ij} as a function of c in the contraction. Passive grid: circles, C'_{11}; squares, C'_{22}. Active grid: diamonds, C'_{11}; triangles, C'_{22}. The solid line is the RDT prediction derived from (2.19), assuming isotropic inlet conditions.

remains constant in the contracting stream. This is consistent with the predictions of RDT (2.18). This shows that the straining is rapid for the large-scale scalar quantities.

Figure 7 shows the fluctuating scalar gradient anisotropy tensor C'_{ij} in the contraction. Also plotted are the RDT predictions given in (2.19), assuming isotropic inlet conditions. For both Reynolds numbers, RDT gives a surprisingly good prediction, considering that the strain rate is fairly low at the small scales. It is interesting to note that the magnitude of both measured components are smaller than predicted by RDT. This is due to the interaction or cross-talk between wavenumber components at the small scales, in contrast to RDT in which the Fourier modes evolve independently. Therefore, RDT overestimates the transverse components and underestimates the longitudinal component.

The scalar dissipation, $\varepsilon^{\theta} = 2\Gamma C_{kk}$, in the contraction is shown in figure 8. The predictions of RDT are also shown using the same assumptions as in figure 7. We see considerably less increase in the thermal dissipation than the predictions of RDT suggest. Here, there are two competing mechanisms: the conduction term seeks to reduce the energy in all components, particularly in the transverse directions, while the net effect of the redistribution term is to channel some of the energy from the transverse components into the longitudinal component.

Figure 9 shows the spectra of the temperature fluctuations at the inlet and the exit of the contraction for both the active and the passive grids, as functions of the initial wavenumber (κ_1°). The spectra, before and after the contraction, are the same at the lower wavenumbers as expected from RDT predictions (2.17). The energy is increased at the higher wavenumbers. The effect is more prominent for the active grid flow than the passive grid, due to the lower strain rate (see figure 4). Note the peak at $\kappa_1^{\circ} \sim 3\,\mathrm{m}^{-1}$ for the active grid flow. This is due to the rotation of the grid bars and does not appear to affect statistics at the inertial and dissipation scales (Mydlarski & Warhaft 1998).

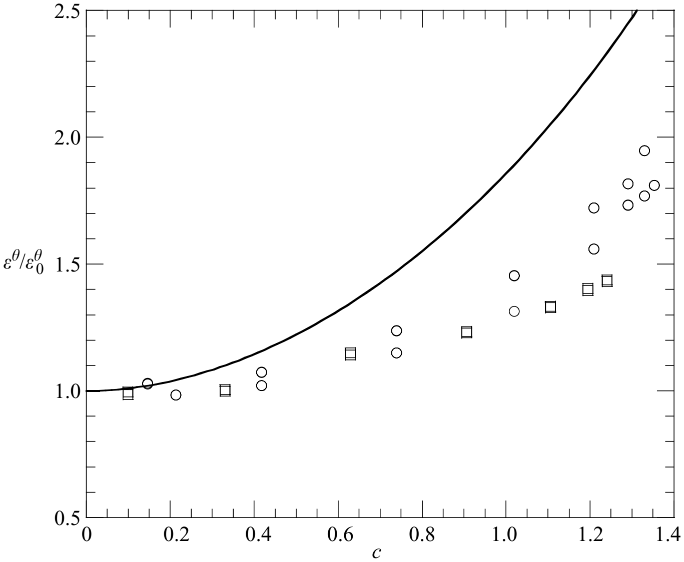

FIGURE 8. The scalar dissipation normalized by the initial scalar dissipation $\varepsilon^\theta/\varepsilon_0^\theta$ as a function of c. Here ε_0^θ is determined at the beginning of the effective straining region, $X/M = -1.0$. Circles: passive grid; squares: active grid. The solid line is the RDT prediction derived from equation (2.19), assuming isotropic inlet conditions.

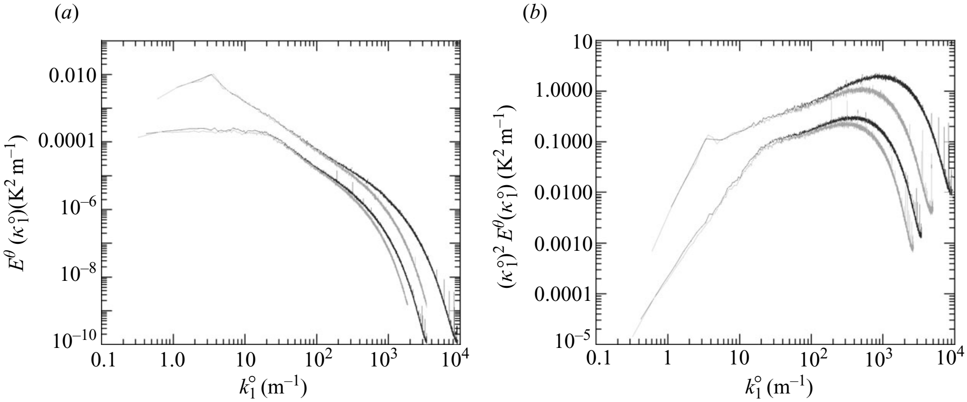

FIGURE 9. (*a*) The one-dimensional temperature fluctuation spectra $E^\theta(\kappa_1^\circ)$ as a function of the initial wavenumber κ_1°. (*b*) The one-dimensional 'dissipation' spectra for the temperature fluctuations $(\kappa_1^\circ)^2E^\theta(\kappa_1^\circ)$ versus κ_1°. For both figures, bottom curves: passive grid; top curves: active grid. The grey lines are the spectra at the inlet of the contraction, while the black lines are spectra at the exit of the contraction.

4.2. *Relaxation region*

As the flow exits the contraction the strain is released and the flow relaxes back towards a more isotropic regime. The return to isotropy of the velocity field has previously been discussed in detail (e.g. see Ayyalasomayajula & Warhaft 2006 and references therein), but less attention has been given to the passive scalar field, although Warhaft (1980) looked at the effect of varying the scalar integral scale and observing its subsequent decay rate after it had been strained.

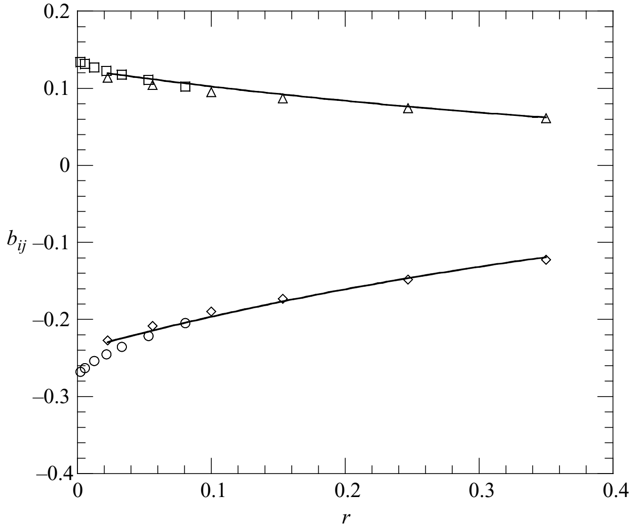

FIGURE 10. The velocity anisotropy tensor b_{ij} in the post-contraction region as a function of time r, defined by $\mathrm{d}r = (k/\varepsilon)\,\mathrm{d}t$, initialized at the end of the effective straining region, $X/M = 5$. passive grid: circles, b_{11}; squares, b_{22}. Active grid: diamonds, b_{11}; triangles, b_{22}. The lines are Rotta's (1951) model predictions, using the value $C_k = 3$ for Rotta's constant.

4.2.1. *Velocity field*

Figure 10 shows the relaxation of the current flow field in terms of the integral time scale. For a detailed discussion about the relaxation of the large-scale flow field, see Ayyalasomayajula & Warhaft (2006).

4.2.2. *Scalar field*

The flow is highly anisotropic as it exits the contraction: the anisotropy and its decay are clearly reflected in the scalar gradients. Figure 11 shows the evolution of the anisotropy tensor for the fluctuating scalar gradient. Also shown in figure 11 is the integral of (2.27), where the unknown parameters $f^{(3)}$, $f^{(4)}$ have been obtained from the active grid measurement, given the evolution of b_{ij} in the same flow. The passive grid flow measurements do not allow for sufficiently accurate estimation of the model constant due to the short evolution. The value of the constants give some idea of relative importance of the terms in the model equation (2.25). Note that to resolve the constant $f^{(2)}$ in (2.25), more detailed measurements are needed. Knowledge of $f^{(2)}$ would allow us to predict the evolution of the scalar dissipation, $2\Gamma C_{kk}$.

Figure 12 shows the relation between the flow time scales and the scalar time scale throughout the whole flow. The ratio between the integral – and the thermal time scale, and the ratio between dissipation – and the thermal time scale, suggest that these scales are intrinsically connected. However the exact relation between the time scale cannot be estimated unless more components of ε^{ζ}_{ij} are measured. The figure also shows the relation between the integral time r and the thermal time s in the relaxation region. With approximately linear relation between the integral time scale τ_l and the thermal time scale τ_ζ (2.27) allows us to resolve the small-scale scalar field from knowledge of the velocity field.

After the contraction, energy is redistributed between the wavenumbers, such that the transverse components lose their energy to the longitudinal ones (e.g. see Ayyalasomayajula & Warhaft 2006). This effect is the strongest at the higher

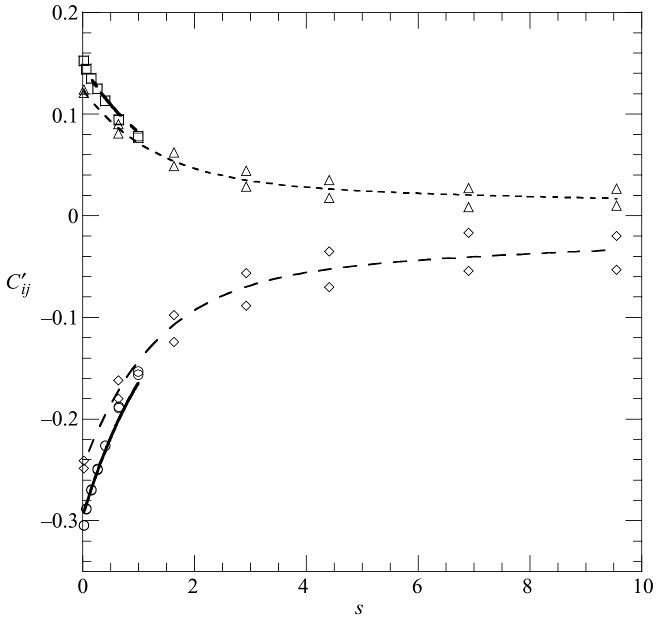

FIGURE 11. The fluctuating temperature gradient anisotropy tensor C'_{ij} versus s in the relaxation region. Passive grid: circles, C'_{11}; squares, C'_{22}. Active grid: diamonds, C'_{11}; triangles, C'_{22}. The lines represent (2.27) with the model constants $f^{(3)}=0.2$ and $f^{(4)}=0.8$. These values were determined via curve fitting of the higher Reynolds number, active grid measurement, resulting in the values $f^{(3)}=0.2\pm0.1$ and $f^{(4)}=0.8\pm0.2$.

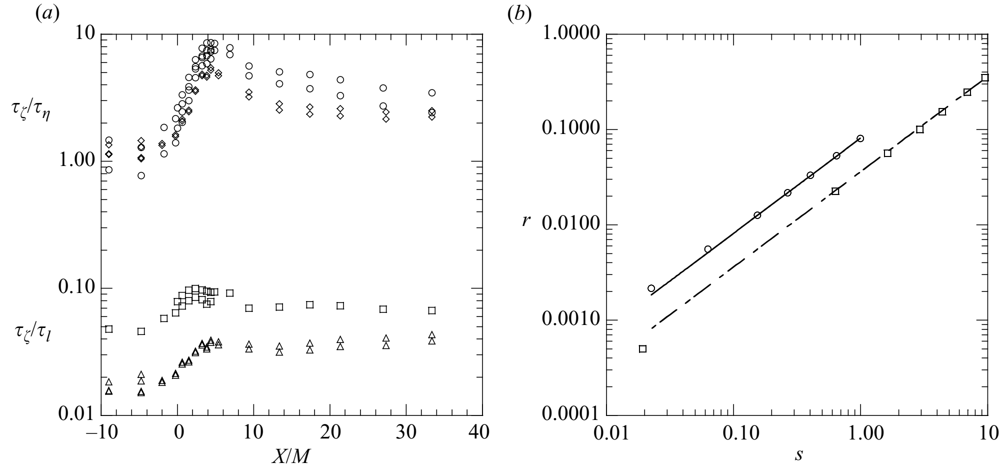

FIGURE 12. (*a*) Ratios between the flow time scales and thermal time scales versus X/M throughout the flow. Circles and diamonds: τ_ζ/τ_η for the passive and active grids respectively; squares and triangles: τ_ζ/τ_l for the passive and active grids respectively. Here, $\tau_\zeta=C_{kk}/\varepsilon^\zeta_{kk}$ is the thermal time, and $\tau_l=k/\varepsilon$ is the integral time. (*b*) The relation between the integral time r and the scalar time s in the relaxation region. Circles: passive grid (curve fit $r=0.081s$, solid line). Squares: active grid (curve fit $r=0.036s$, dashed line).

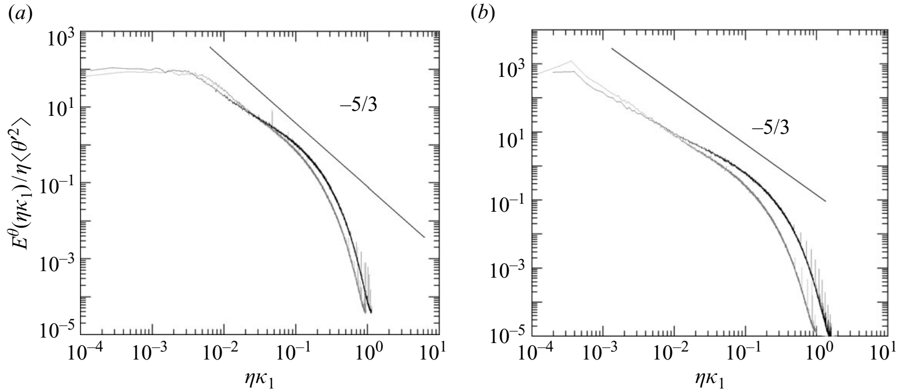

FIGURE 13. The normalized one-dimensional spectra for the temperature fluctuations $E^{\theta}(\eta\kappa_1)/\eta\langle\theta'^2\rangle$ versus $\eta\kappa_1$. (*a*) Passive grid; (*b*) active grid. Grey lines: immediately after contraction (at $X/M = 5$); black lines: At $X/M = 33.4$. The solid straight lines have $-5/3$ slope.

wavenumbers, since the redistribution is most effective at the small length scales, due to the small time scales. To demonstrate this dynamic effect, figure 13 shows the one-dimensional spectra in κ_1 just after the straining region and further downstream. There is a significant increase in the energy at the higher wavenumbers, extending well into the inertial range. This 'bump' has the effect of decreasing the slope of the spectrum. Presumably the $-5/3$ slope would be recovered if the flow were allowed a longer evolution time.

4.3. *Model applied to the straining region*

We have used the experimental results obtained in the relaxation region to determine values for the model constants in (2.27) at the given Reynolds and Prandtl numbers. In figure 14 we show how the extended model, presented in (2.28), performs in the straining region. The equation has been numerically integrated using the known evolution of the velocity field. The graph shows that the model performs considerably better than the RDT prediction presented in figure 7. Included in figure 14 is a comparison, when the model constants in (2.28) are set to zero.

5. Conclusions

The effects of straining on a passive scalar field in turbulent flow was investigated and compared with the RDT predictions. The strain rate is such that the large scales statistics are found to be well predicted by RDT, while the small scales are found to deviate from RDT due to the nonlinear terms ignored by RDT.

After the flow exited the straining region, we investigated its relaxation to a more isotropic state. We have successfully derived a simple tensor model that predicts the evolution of the thermal fluctuations from a highly anisotropic initial condition to a more relaxed (but not isotropic) state. The relaxation manifests itself initially in the scalar spectra as a 'bump' at the higher wavenumbers due to the redistribution at the smallest scales. This was also observed in the velocity field (Ayyalasomayajula & Warhaft 2006)

The model was shown to apply to the straining region as well as to the relaxation region, suggesting that it may be useful in flows in which RDT is not accurate.

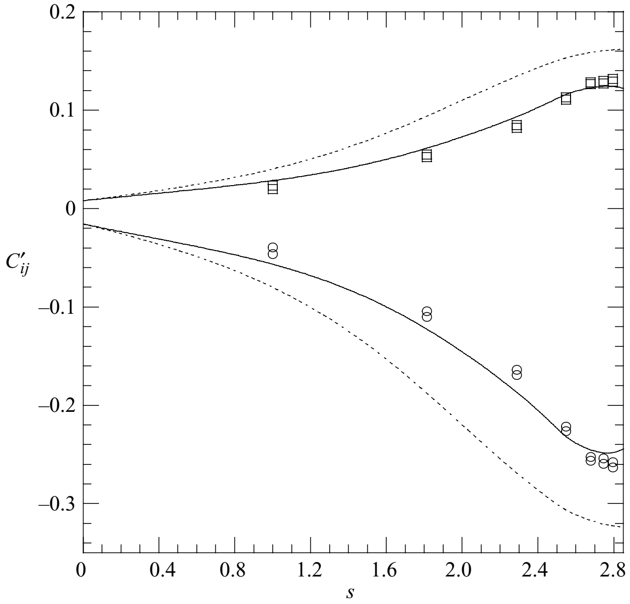

FIGURE 14. The fluctuating temperature gradient anisotropy tensor C'_{ij} versus s in the straining region for the active grid measurement. Here, $s=0$ and $s=2.85$ refer to the beginning and the end of the effective contraction. Circles: C'_{11}; squares: C'_{22}. The solid lines represent numerical integration of (2.28) for both C'_{11} and C'_{22}, using the model constants from figure 11. The dashed lines represent integration of (2.28) when the model constants are set to zero.

Application of the model requires that the relation between the mechanical and the thermal time scales is known. However we suggest that for higher strain rates the evolution of the scalar dissipation is well predicted by RDT (figure 7).

We thank S. B. Pope for discussions about the modelling and S. Ayyalasomayajula for his insights and help with the experiment. This work was funded by the US National Science Foundation.

REFERENCES

AYYALASOMAYAJULA, S. & WARHAFT, Z. 2006 Nonlinear interactions in strained axi-symmetric high-Reynolds-number turbulence. *J. Fluid Mech.* **566**, 273–307.

BATCHELOR, G. K 1953 *The Theory of Homogeneous Turbulence*. Cambridge University Press.

BILGER, R. W. 2004 Some aspects of scalar dissipation. *Flow Turb. Combust.* **72** (2), 93–114.

CHUNG, M. K. & KIM, S. K. 1995 A nonlinear return-to-isotropy model with Reynolds-number and anisotropy dependency. *Phys. Fluids* **6**, 1425–1437.

COMTE-BELLOT, G. & CORRSIN, S. 1966 The use of a contraction to improve the isotropy of grid-generated turbulence. *J. Fluid Mech.* **25**, 657–682.

DIMOTAKIS, P. E. 2005 Turbulent mixing. *Annu. Rev. Fluid Mech.* **37**, 329–356.

GYLFASON, A., AYYALASOMAYAJULA, S. & WARHAFT, Z. 2004 Intermittency, pressure and acceleration statistics from hot-wire measurements in wind-tunnel turbulence. *J. Fluid Mech.* **501**, 213–229.

GYLFASON, A. & WARHAFT, Z. 2004 On higher order passive scalar structure functions in grid turbulence. *Phys. Fluids* **16**, 4012–4019.

HANJALIC 1994 Advanced turbulence closure models: a view of current status and future prospects. *J. Heat Fluid Flow* **15**, 178–203.

HUNT, J. C. R. & CARRUTHERS, D. J. 1990 Rapid distortion theory and the problems of turbulence. *J. Fluid Mech.* **212**, 497–532.

Launder, B. E., Reece, G. J. & Rodi, W. 1975 Progress in development of a Reynolds-stress turbulent closure. *J. Fluid Mech.* **68**, 537–566.

Lumley, J. L. & Newman, G. R. 1977 Return to isotropy of homogeneous turbulence. *J. Fluid Mech.* **82**, 161–178.

Makita, H. 1991 Realization of a large-scale turbulence field in a small wind tunnel. *Fluid Dyn. Res.* **8**, 53–64.

Meneveau, C. & Katz, J. 2000 Scale-invariance and turbulence models for large-eddy simulation. *Annu. Rev. Fluid Mech.* **32**, 1–32.

Mydlarski, L. & Warhaft, Z. 1996 On the onset of high Reynolds number grid-generated wind-tunnel turbulence. *J. Fluid Mech.* **320**, 331–368.

Mydlarski, L. & Warhaft, Z. 1998 Passive scalar statistics in high-Péclet-number grid turbulence. *J. Fluid Mech.* **358**, 135–175.

Newman, G. R., Launder, B. E. & Lumley, J. L. 1981 Return to isotropy of homogeneous turbulence. *J. Fluid Mech.* **111**, 135–232.

O'Young, F. & Bilger, R. W. 1997 Scalar gradient and related quantities in turbulent premixed flame. *Combust. Flames* **109** (4), 682–700.

Peters, N. 1983 Local quenching due to flame stretch and non-premixed turbulent combustion. *Combust. Sci. Tech.* **30**, 1–17.

Pope, S. B. 1990 Computations of turbulent combustion: progress and challenges. In *23rd Symp. on Combustion*, Pittsburg, PA.

Pope, S. B. 2000 *Turbulent Flows*. Cambridge University Press.

Prandtl, L. 1933 Attaining a steady air stream in wind tunnels. *TM* **726**, NACA.

Rahai, H. R. & LaRue, J. C. 1995 The distortion of passive scalar by two-dimensional objects. *Phys. Fluids* **7** (1), 98–107.

Reynolds, W. C. & Kassinos, S. C. 1995 One-point modelling of rapidly deformed homogeneous turbulence. *Proc. R. Soc. Lond.* A **451**, 87–104.

Rogers, M. M. 1991 The structure of a passive scalar field with a uniform mean gradient in rapidly sheared homogeneous turbulent flow. *Phys. Fluids* **3** (1), 144–154.

Rotta, J. 1951 Statistische theorie nichthomogener turbulenz. *Z. Phys.* **129**, 547–572.

Savill, A. M. 1987 Recent developments in rapid-distortion theory. *Annu. Rev. Fluid Mech.* **19**, 531–575.

Sirivat, A. & Warhaft, Z. 1983 The effect of a passive cross-stream temperature gradient on the evolution of temperature variance and heat flux in grid turbulence. *J. Fluid Mech.* **128**, 326–346.

Taylor, G. I. 1933 Turbulence in a contracting stream. *Zeit. Angew. Math. Mech.* **15**, 91–96.

Tennekes, H. & Lumley, J. L. 1972 *A First Course in Turbulence*. MIT Press.

Townsend, A. A. 1976 *The Structure of Turbulent Shear Flow*. Cambridge University Press.

Warhaft, Z. 1980 An experimental study of the effect of uniform strain on thermal fluctuations in gridgenerated turbulence. *J. Fluid Mech.* **99**, 545–573.

Warhaft, Z. 2000 Passive scalars in turbulent flows. *Annu. Rev. Fluid Mech.* **32**, 203–240.

Wyngaard, J. C. 1988 The effects of probe-induced flow distortion on atmospheric turbulence measurements: extension to scalars. *J. Atmos. Sci.* **45**, 3400.